nature electronics

Article

https://doi.org/10.1038/s41928-023-01000-3

Biphasic quasistatic brain communication for energy-efficient wireless neural implants

Received: 9 May 2022

Accepted: 30 June 2023

Published online: 31 August 2023

Check for updates

Baibhab Chatterjee[1,5,2] ✉, Mayukh Nath[1], Gaurav Kumar K[1], Shulan Xiao[3], Krishna Jayant[2,3,4] & Shreyas Sen[1,2,3] ✉

Wearable devices typically use electromagnetic fields for wireless information exchange. For implanted devices, electromagnetic signals suffer from a high amount of absorption in tissue, and alternative modes of transmission (ultrasound, optical and magneto-electric) cause large transduction losses due to energy conversion. To mitigate this challenge, we report biphasic quasistatic brain communication for wireless neural implants. The approach is based on electro-quasistatic signalling that avoids transduction losses and leads to an end-to-end channel loss of only around 60 dB at a distance of 55 mm. It utilizes dipole-coupling-based signal transfer through the brain tissue via differential excitation in the transmitter (implant) and differential signal pickup at the receiver (external hub). It also employs a series capacitor before the signal electrode to block d.c. current flow through the tissue and maintain ion balance. Since the electrical signal transfer through the brain is electro-quasistatic up to the several tens of megahertz, it provides a scalable (up to 10 Mbps), low-loss and energy-efficient uplink from the implant to an external wearable. The transmit power consumption is only 0.52 μW at 1 Mbps (with 1% duty cycling)—within the range of possible energy harvesting in the downlink from a wearable hub to an implant.

The advancement of scientifically and societally critical applications such as brain–machine interfaces, electroceuticals and connected healthcare relies on implantable or injectable devices with an extremely small form factor[1,2]. In practice, these would be placed within the central and peripheral nervous systems of freely moving subjects. The technology, thus, requires self-sustained, energy-efficient and secure mechanisms for information exchange[3,4]. Conventional neural interfaces use tethered communication for data transmission and power (Fig. 1a)[5]. However, such wired connections increase the risks of cortical scarring, gliosis, infection and leakage of the cerebrospinal fluid (CSF). Therefore, there has been a considerable amount of research interest to develop wireless neural implants (Fig. 1b), and the future of such brain implants is envisioned[6] to consist of a network of self-sufficient, untethered multichannel implants/nodes, utilizing wireless communication and powering (Fig. 1c).

A variety of miniaturized wireless neural sensors[7–9] and stimulators[10–12]—using a range of data and power transmission modalities—have previously been developed (Fig. 2a–c). Among these modalities, radio-frequency (RF) systems[7,13] suffer from increased tissue absorption at high frequencies, and require large transmitter power (0.5 W, for example[7,13], which exceeds the International Commission on Non-Ionizing Radiation Protection (ICNIRP) safety guidelines[14–16] by around ten times). Optical[8] and ultrasonic[9] telemetry are safer, but they suffer from considerable loss due to scattering and skull absorption (110 dB loss, for example[9]); this reduces end-to-end efficiency and means that a sub-cranial interrogator, which is surgically placed,

[1]Elmore Family School of Electrical and Computer Engineering, Purdue University, West Lafayette, IN, USA. [2]Center for Internet of Bodies (C-IoB), Purdue University, West Lafayette, IN, USA. [3]Weldon School of Biomedical Engineering, Purdue University, West Lafayette, IN, USA. [4]Purdue Institute for Integrative Neuroscience, Purdue University, West Lafayette, IN, USA. [5]Present address: Department of Electrical Engineering, University of Florida, Gainesville, FL, USA. ✉e-mail: bchatte@purdue.edu; shreyas@purdue.edu

https://doi.org/10.1038/s41928-023-01000-3

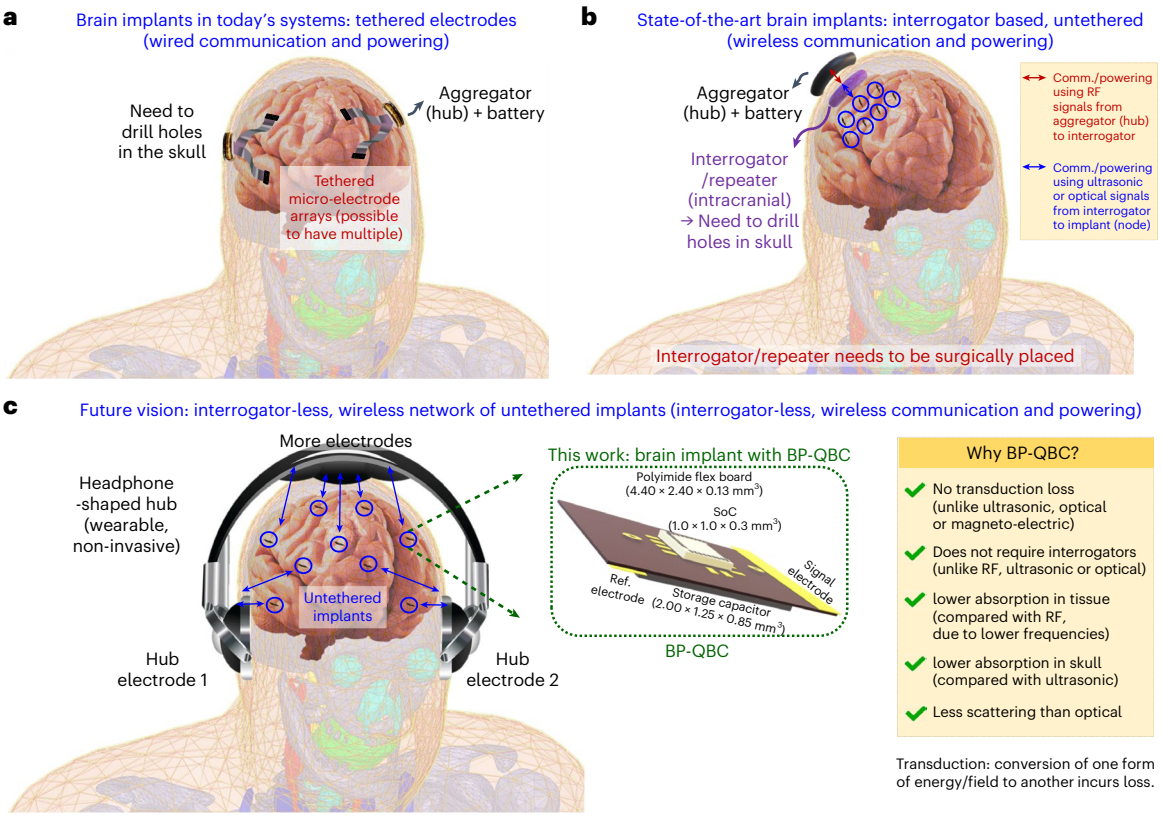

Fig. 1 | Need for wireless communication in brain implants. a, Wired/tethered communication and powering in today's brain implants (the example devices shown here are inspired by Neuralink v. 2.0 (ref. 5)), where the electrodes are placed inside the brain by drilling holes on the skull. The data aggregator/hub, separate communication devices and a battery can be packaged together and utilized to fuse the hole in the skull and connecting with the external world. **b**, State-of-the-art brain implants with interrogator/repeaters surgically placed in the sub-cranial region that communicate wirelessly with the implanted nodes using optical/ultrasound techniques. **c**, Proposed untethered BP-QBC for data communication and powering in grain-sized nodes, sprinkled throughout the brain, which communicate with a headphone-shaped wearable hub. The vision for future brain implants include a network of untethered multichannel implants/nodes, enabled by wireless communication and powering. Elements of the human figures created with the human model from ref. 46, which was also used for electro-quasistatic simulations in this Article. Brain images from Pixabay.com.

needs to be used to improve the quality of the signal (Fig. 1b). Alternatively, the magneto-electric technique[10] has low tissue absorption but also suffers from high transduction loss (a 0.1 mT magnetic-field requirement[10], which is equivalent to around 300 kV m^{-1} electric field for iso-energy density).

In this Article, we report a wireless communication approach for neural implants termed biphasic quasistatic brain communication (BP-QBC) that offers wireless communication and powering without a sub-cranial interrogator (Fig. 2b–f). In this approach, the implant can sense and transmit information to a wearable headphone-shaped hub through the uplink (Fig. 1c). The hub sends power and configuration/programming bits to the implant through the downlink. Both uplink and downlink use fully electrical signals to avoid transduction losses (a challenge in optical, ultrasound and magneto-electric systems). In particular, the uplink uses narrow-band electro-quasistatic (EQS) frequencies ranging from tens of kilohertz to tens of megahertz (with an option of increasing the frequency to around 1 GHz) to avoid interfering with physiological signals and potentially avoid stimulating or inhibiting the brain tissue with low frequencies.

Human body communication (HBC) has previously been shown to conduct electrical signals through the tissue. With traditional capacitive human body communication (C-HBC) and in the ideal scenario (with no geometric/positional imbalance[17]), the capacitive return path required for signal transmission is not separately present for an implanted transmitter to Earth's ground, leading to almost zero received voltages[18]. For galvanic human body communication (G-HBC), on the other hand, the electrodes on the implant are almost shorted through the low-impedance (around hundreds of ohms to a few kilo-ohms) tissue/fluids in the body, resulting in high d.c. power consumption. In our BP-QBC method, a d.c.-blocking capacitor in the signal path creates a biphasic output for communication that eliminates the d.c. power going into the tissue and maintains ion balance in the channel. Although biphasic signals have been commonly used for neural stimulation, this work demonstrates the advantage of biphasic data transmission through the brain tissue for communicating with a deep neural implant.

EQS brain communication: fundamentals

At low frequencies (several tens of megahertz or less), transmission through the tissue can be approximated to be EQS in nature, as the wavelength is larger than the channel lengths. The potential difference created by the magnetic fields is usually ignored since no closed current loops exist at the transmitting or receiving electrodes, and the phase of the signal in the channel remains almost constant. The relation between the magnitudes of the developed electric field ($\vec{E}$) and the approximation error ($\vec{E}_{\text{error}}$) during data transmission[19,20] for a particular EQS frequency ($f = \frac{\omega}{2\pi}$) is given as

$$\vec{E} = \vec{E}_{\text{EQS}} + \vec{E}_{\text{error}}, \frac{E_{\text{error}}}{E} = \omega^2 \mu_{\text{tissue}} \epsilon_{\text{tissue}} r^2. \quad (1)$$

In equation (1), r represents the dimension of the transmitting electrode for EQS HBC (<1 cm) and ε and μ denote the permittivity and

https://doi.org/10.1038/s41928-023-01000-3

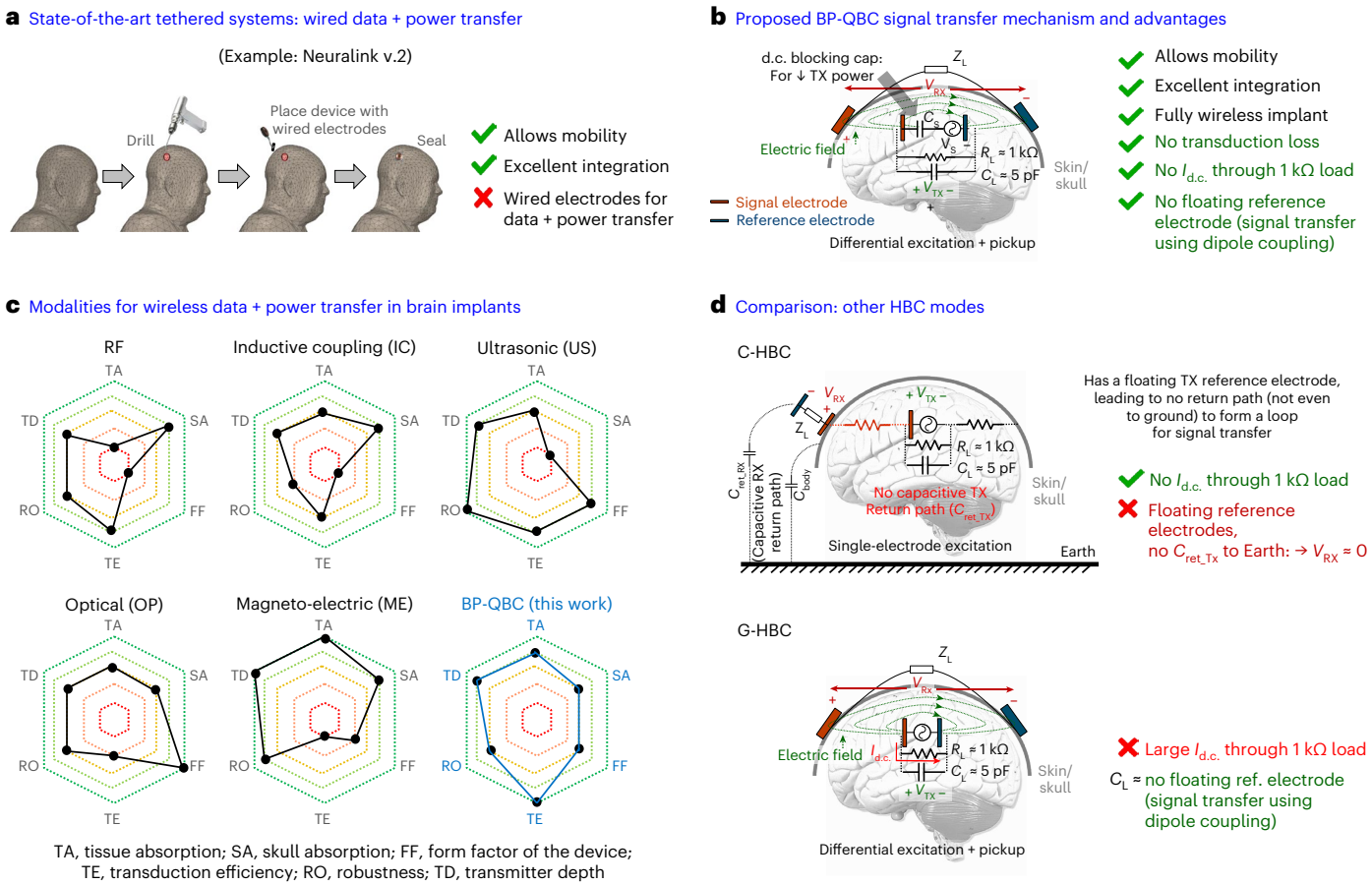

Fig. 2 | System-level analysis of BP-QBC versus other available methods. **a**, Surgical process of drilling holes in the skull to place state-of-the-art wired brain implants (an example is shown, describing the techniques adopted by Neuralink v. 2.0 (ref. 5)). **b**, Wireless signal transfer mechanism of the proposed BP-QBC modality, along with its advantages. **c**, State-of-the-art wireless brain implants with untethered communication and powering, showing a performance comparison with RF, inductive coupling, ultrasonic, optical, magneto-electric and the proposed BP-QBC techniques, demonstrating the high transduction efficiency with low tissue/skull absorption, large transmitter depth and reasonable form factor in addition to robustness for BP-QBC. **d**, Comparison of the signal transfer mechanism with other HBC modalities. Specifically, comparison with C-HBC and G-HBC is performed. **e**, Implementation of the 5 mm^3 BP-QBC SoC (ref. 44) for wireless powering and data transfer from a brain implant (node) to an external headphone-shaped hub placed on the skull/skin. **f**, System architecture of the wearable hub and the neural implant (node). The hub contains an uplink data receiver, a downlink data transmitter and a downlink power transmitter. The node contains an uplink data transmitter, a downlink data receiver and a downlink power receiver for communication and powering. Panels **b**, **e** and **f** adapted with permission from ref. 44, IEEE. Elements of the human figures created with human models from ref. 46 and MakeHuman[51]. Brain images from Pixabay.com.

permeability, respectively, of the conductive tissue (in the brain). The maximum relative permittivity (for the worst case, at very low frequencies such as kilohertz) of the brain tissue is about 3,000 (refs. 21,22). The near-field quasistatic approximation ($\vec{E} \approx \vec{E}_{EQS}$) holds true as long as the magnitude of $E_{error} \ll E$, which implies

$$\omega^2 \mu_{tissue} \epsilon_{tissue} r^2 \ll 1, \epsilon_{tissue} \approx 3,000 \epsilon_{air}, \mu_{tissue} \approx \mu_{air}, \quad (2)$$

$$f \ll \frac{1}{2\pi r \sqrt{\mu_{tissue} \epsilon_{tissue}}} \approx 87.11\,\text{MHz}. \quad (3)$$

This means that the intensity of the electromagnetic fields radiated is dominated by the quasistatic near field[22], as long as $f \ll 87.11$ MHz, considering $c = 3 \times 10^8$ m s^{-1} to be the velocity of propagation of

electromagnetic waves in air. However, it must be kept in mind that biological tissue is dispersive, and hence, the threshold frequency could vary. In this work, unless otherwise stated, we employ a transmission frequency of 1 MHz, thereby allowing the EQS field as the dominant mode of signal propagation through the brain, with an insubstantial approximation error of $\left(\frac{1.00\,\text{MHz}}{87.11\,\text{MHz}}\right)^2 \times 100 = 0.013\%$.

In the EQS range, wearable HBC devices commonly utilize a capacitive signal transfer mechanism[23–39], where the transmitter excites the human body using a single-ended electrode, and the receiver picks up the signal from a different point on the body using another single-ended electrode. Since there is no common reference between the transmitter and receiver, the signal transfer mechanism becomes a function of the return-path capacitances between (1) the transmitter and Earth's ground and (2) the receiver and Earth's ground. Biophysical models for C-HBC were developed in our earlier works[18,34], where the effects of these capacitances on the overall channel transfer function (TF) were analysed, which was found to be proportional to the return-path capacitances at both transmitter and receiver. The effect of moving the transmitter device within the body (for an implant) was also analysed[18], which showed that the return-path capacitance for the implanted transmitter becomes almost zero, as the electric fields terminate within the body, and cannot terminate to Earth's ground as in the wearable scenario. Due to the absence of a transmitter return-path capacitance, the received voltage is almost zero (Fig. 2d shows an example for a brain implant). However, due to certain geometrical and positional asymmetries in any realistic device[17], some amount of voltage is generally observed at the receiver, but the channel loss is usually as high as 80–100 dB. Interestingly, due to the presence of only one electrode (single-ended excitation), there is no d.c. path from the signal electrode to the reference electrode in the transmitter even if the signal is not d.c. balanced.

On the other hand, the galvanic mode of signal transfer[17,40–43] has been shown to work better for implants, where the transmitter uses differential (galvanic) excitation, and the signal pickup at the receiver is also differential. As shown in Fig. 2d, part of the electric fields going from the signal electrode to the reference electrode in the transmitter is available at the receiving electrodes for G-HBC. However, the human tissue (brain, in this scenario) presents itself as a low-resistance load (about 1 kΩ or less) between the signal and reference electrodes of the transmitter[44]. If the transmit signal is not d.c. balanced (usually the case for traditional G-HBC), this will result in a large amount of d.c. power in the implant.

To simultaneously leverage the advantages of C-HBC and G-HBC, we present BP-QBC, which utilizes differential electrodes at both transmitter and receiver for a signal transfer mechanism similar to G-HBC, but also employs a series capacitor before the signal electrode to prevent any d.c. current flow into the brain tissue (Fig. 2b). Being fully EQS, BP-QBC does not suffer from transduction losses that affect competing wireless techniques (optical/ultrasonic/magneto-electric). At the same time, unlike RF, BP-QBC signals are not absorbed as much in the brain tissue because of the lower frequencies. Moreover, there is no requirement of large coils as in RF/inductive techniques. Furthermore, due to the low end-to-end system loss due to no field transduction, there is no need for sub-cranial interrogators/repeaters to boost the signal, as generally observed in optical and ultrasonic systems, making the proposed BP-QBC technique amenable to the vision of interrogator-less, wireless network of implants (Fig. 1c).

BP-QBC: device and system design

The system architecture for the wearable headphone-shaped hub and the BP-QBC-enabled brain implant is shown in Fig. 2f. The wearable hub contains an uplink data receiver, a downlink data transmitter and a downlink power transmitter, whereas the brain implant consists of an uplink data transmitter, a downlink data receiver, a biphasic stimulator and energy-harvesting modules. Communication from the node to the hub forms the uplink, whereas communication from the hub to the node forms the downlink. To properly characterize the BP-QBC signal transmission properties across different frequencies and channel lengths, an extremely small-sized (a few cubic millimetres or less) transmitter is required as an implant, which can sweep across kilohertz–gigahertz frequencies. Furthermore, the ground isolation requirements[18,31,34] in an HBC transmitter demands the device to be self-sustained and not plugged into any ground-connected power/signal source or measurement device. Due to such stringent volume, energy and ground isolation requirements of a realistic brain implant, the core circuitry of the node in the said architecture is implemented in the form of a 0.3 mm^3 custom-designed integrated circuit (IC), which can sweep across different frequencies, unlike commercially available signal sources. The details of the custom-designed IC can be found in our recent work[44]. Figure 3a exhibits the die micrograph of our implemented IC, whereas Fig. 3b shows a conceptual diagram of the flexible printed circuit board (PCB) implemented with polyimide as a brain implant in this work. The PCB consists of the 0.3 mm^3 IC and a signal electrode on the front side, with a less than 3 mm^3 storage capacitor and a reference electrode on the back side. Placing the electrodes on two different sides of the PCB helps in maximizing the distance between the transmitting electrodes in the uplink, which is beneficial in terms of the channel TF (as discussed later in this section). The node can sense the input signals, and can communicate using BP-QBC as well as G-HBC. For the rest of this Article, we shall mostly focus on the scientific mechanism of BP-QBC, and support it with theory and measurements.

The electrical signal transfer properties in the human brain are shown in Fig. 3c, which exhibits the relative permittivity and conductivity of brain tissue (both grey matter and white matter) as a function of frequency, showing that the tissue has a higher permittivity at low frequencies (kilohertz–megahertz), which means that the signal transfer through the tissue mostly happens through the creation of electric fields (dipole coupling where differential excitations are involved). The brain tissue has a high conductivity at higher frequencies (about 1 GHz or more), where the signal transfer will happen mostly through electrical currents. However, at such frequencies, the EQS approach does not hold true, and requires considerations on signal reflection, constructive/destructive interference and absorption of electromagnetic fields in the tissue.

To develop an intuitive understanding of the signal transfer mechanism and channel loss, we modelled the channel TF using the theory of dipole coupling in three-dimensional space. The channel TF as a function of uplink transmitter and receiver geometries is shown in equation (4). A complete derivation of equation (4) is available in Supplementary Note 1 (Supplementary Fig. 1 provides the analysis).

$$\text{TF} = Q_{\text{CD}}\left[\frac{1}{r_{\text{CA}}-r_{\text{e,C}}} - \frac{1}{r_{\text{CB}}-r_{\text{e,C}}} - \frac{1}{r_{\text{DA}}-r_{\text{e,D}}} + \frac{1}{r_{\text{DB}}-r_{\text{e,D}}}\right] / Q_{\text{AB}}\left[\frac{1}{r_{\text{e,A}}} - \frac{1}{r_{\text{AB}}-r_{\text{e,A}}} - \frac{1}{r_{\text{AB}}-r_{\text{e,B}}} + \frac{1}{r_{\text{e,B}}}\right], \quad (4)$$

where A, B, C and D are the centre points of the signal electrode in the node transmitter, reference electrode in the node transmitter, signal electrode in the hub receiver and reference electrode in the hub receiver, respectively (Fig. 3d and Supplementary Fig. 1); r_{XY} represents the linear distance between points X and Y (for example, r_{CA} is the linear distance between points C and A); and $r_{\text{e,X}}$ represents the radius of the electrode with a centre point at X (for example, $r_{\text{e,A}}$ is the radius of the signal electrode in the transmitter). Also, Q_{AB} and Q_{CD} are the effective EQS charges between the transmitting and receiving electrodes, respectively. Please note that the channel TF is purely a function of the geometries, and is independent of frequency, as expected in the EQS regime. Equation (4) is further validated with finite element method (FEM)-based simulations in Ansys high-frequency structure simulator

https://doi.org/10.1038/s41928-023-01000-3

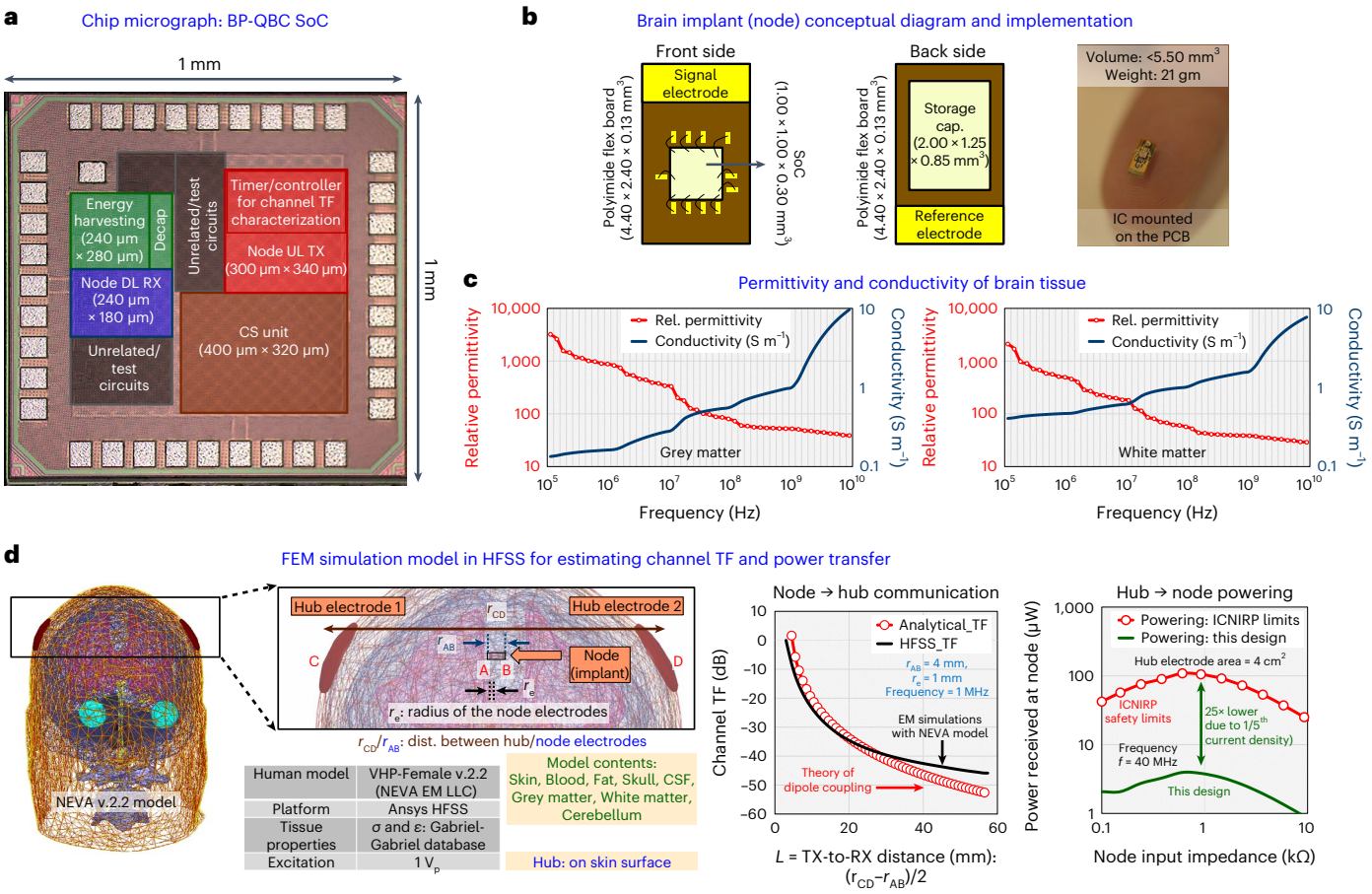

Fig. 3 | Implementation and modelling of BP-QBC. a, Die micrograph of the BP-QBC SoC, showing energy-harvesting modules, node uplink data transmitter as well as node downlink data and power receivers. **b**, Conceptual diagram of the SoC, placed on a flexible polyimide PCB. **c**, Relative permittivity and conductivity of brain tissue (both grey matter and white matter are shown) as a function of frequency, showing that tissue has a higher permittivity at low frequencies (kilohertz–megahertz), which means that signal transfer through the tissue mostly happens through the creation of electric fields (dipole coupling where differential excitations are involved). The brain tissue has a high conductivity at higher frequencies (~1 GHz or more), where the signal transfer happens mostly through electrical currents. However, at such frequencies, the EQS approach does not hold true, and requires considerations on signal reflection and constructive/destructive interference. **d**, FEM-based modelling using HFSS, showing the channel TF for communication and powering for the device sizes of interest. The simulation results with a human model from NEVA EM LLC[46] shows excellent correspondence between the simulation results and theory of dipole coupling for the channel TF. When a 40 MHz current excitation is used for powering, with current levels at one-fifth the ICNIRP safety limits[14–16] (that is, 40 mA cm^{-2} from the hub), about 4 µW of power is available at the implant. **e**, FEM simulation results showing the creation of ~100× stronger electric fields within the brain when powered from a hub with differential excitation compared with a hub with single-ended excitation for powering. Panels **a**, **b** and **d** adapted with permission from ref. 44, IEEE.

(HFSS), and the simulation results as a function of the channel length match closely with the analytical expression (Fig. 3d). For a channel length of about 50–60 mm (realistic worst-case distance between a human brain implant and the hub electrodes), the loss is around 60 dB from both analytical expressions and HFSS simulations. The channel TF for (1) various electrode separation (r_{AB}) and (2) various electrode radii ($r_{e,A} = r_{e,B}$) of the uplink transmitter (implant) are plotted in Fig. 4a,b, showing excellent conformity between the theory and simulation results. The receiving electrode size does not have a noteworthy effect on signal transfer as the channel length is usually much higher

https://doi.org/10.1038/s41928-023-01000-3

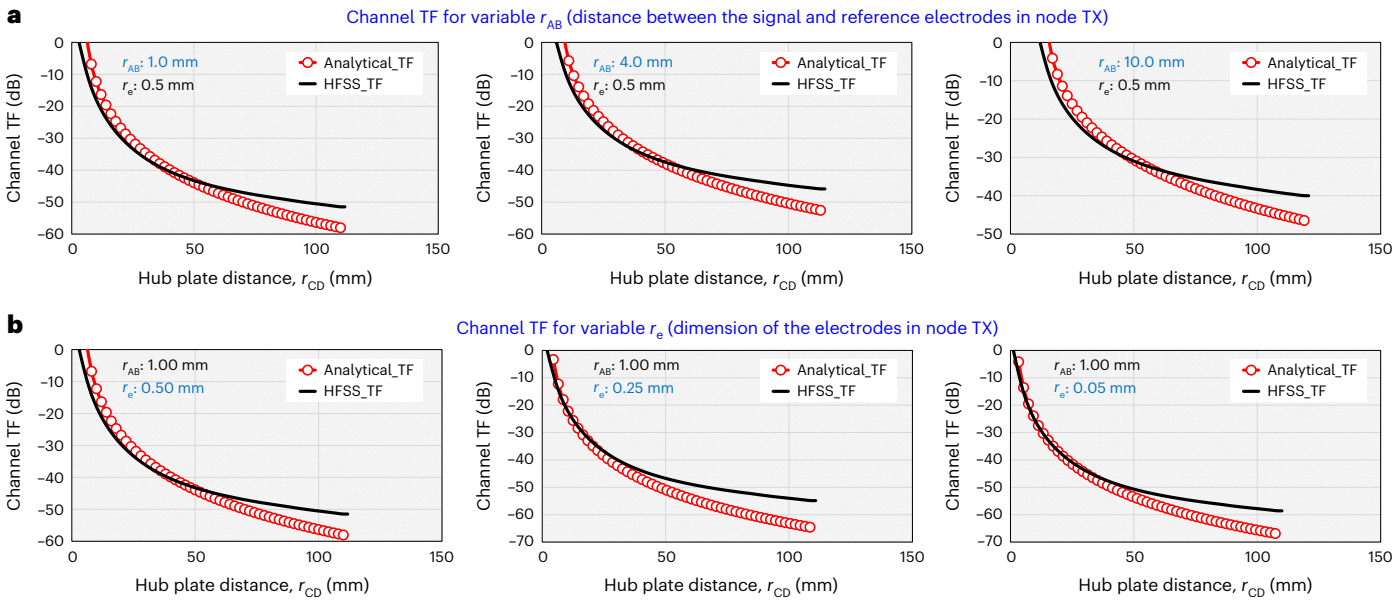

Fig. 4 | Channel TF for the BP-QBC implant. a, Channel TF with variable distances between the transmitter electrodes (r_{AB}), using both analytical expressions (red, circular marker) and HFSS simulations (black, no marker) with the human head model from NEVA EM LLC[46]. **b**, Channel TF with variable dimensions/radii of the transmitter electrodes ($r_{e,A}$), using both analytical expressions (red, circular marker) and HFSS simulations (black, no marker) with the human head model from NEVA EM LLC[46].

than the electrode size. This was separately validated in the simulation. Please note that for the analysis presented above, the implant is assumed to be equidistant from the hub electrodes, which results in a worst-case TF due to positional (as well as geometric) symmetry. For all the other cases, the received signal will be higher, facilitating the signal transfer. However, for the current analysis, it is also assumed that the implant and hub electrodes are perfectly aligned. This, however, results in the maximum received signal. To ensure such an alignment of electrodes for all the implants in the brain (even for the ones tilted at an angle), a skull cap with multiple electrodes can be used as the wearable hub for better signal quality at the receiver in more realistic scenarios.

The hub can also transfer power to the brain implant by differentially exciting the tissue using EQS signals (Fig. 3e). According to the ICNIRP safety guidelines[14], a 40 MHz differential current excitation of 8 mA cm^{-2} is used, which is one-fifth the safety limits at 40 MHz (within the EQS range). Such differential excitation results in more than 100× higher electric fields within the brain tissue compared with single-ended excitation (Fig. 3e), and this results in ~4 μW of available power at the implant with a size of ~5 mm^3, when the implant's input impedance is matched near the tissue impedance (Fig. 3d).

Channel TF and power consumption measurements

The main goal of performing the following experiments is to analyse the BP-QBC TF for in vitro/in vivo channels as a function of the frequency and implant-to-hub distance. The simplified block diagram of the custom IC used for this purpose is shown in Fig. 5a, which has the capability of sweeping frequencies in the kilohertz–gigahertz range.

Figure 5b shows the in vitro measurement setup and methods for characterizing the BP-QBC channel TF as a function of (1) frequency and (2) implant-to-hub distance. The custom IC, capable of sweeping frequencies in the range of 40 kHz to 1 GHz, is placed on a flexible PCB, and is tested in both phosphate-buffered saline (PBS) environment, and using brain slices from a C57BL/6J mouse. Figure 5c shows the channel TF as a function of channel length (L is the implant-to-hub distance), exhibiting about 30 dB loss for L = 10 mm and about 55 dB loss for L = 60 mm at a frequency of 1 MHz. For the experiments with the mouse brain slice in artificial CSF, L is limited to around 10 mm due to the size of the brain slice. However, both experiments with PBS and brain slice demonstrate similar channel TF as a function of channel length L. Also, there is no major discontinuity as the receiver moves from inside the bowl to the outside, because in the EQS range of frequencies, the channel TF is primarily a function of geometries and transmitter-to-receiver distance, and not a strong function of the material. Figure 5d shows the channel TF as a function of frequency for two scenarios: (1) with PBS (L = 60 mm) and (2) with the mouse brain slice (L = 10 mm). The channel below the 100 MHz range is almost flat band, with a channel loss of about 55 dB for L = 60 mm and a channel loss of about 30 dB for L = 10 mm. The flat-band nature of the channel is consistent with the dipole coupling theory presented earlier in equation (4) for EQS communication. At higher frequencies (>100 MHz), the transmit electrodes start working as better antennas, and the brain tissue/PBS start becoming more conductive, leading to a lower channel loss (Fig. 5d, right). However, at these frequencies, the signal transfer mechanism starts deviating from EQS, and becomes more electromagnetic, thereby leading to more radiation and tissue absorption. As shown in Fig. 5e, the power consumption of the IC without any duty cycling was around 11 μW at 1 MHz for both PBS and brain slice experiments. Finally, Fig. 5f shows the angle sensitivity of the data link during uplink communication, showing about 7.5 dB worst-case degradation in channel voltage TF in simulation, and around 6.0 dB worst-case degradation in channel voltage TF for in vitro measurements, when the line joining the implant electrodes is at a 90° angle with the line joining the hub electrodes. For the in vitro measurements, once the implant is submerged in PBS, we only move the location of the receiver (hub) electrodes to change the angle with the implant, to create minimum disturbance to the submerged node.

Figure 6a shows the in vivo measurement setup and methods for demonstrating the BP-QBC signal transfer and measure the power consumption of the device. The PCB carrying the IC is placed on the brain of a live C57BL/6J mouse. Figure 6b shows the two modes that the IC (implant/node) can be configured: (1) G-HBC mode and (2) BP-QBC mode. In the G-HBC mode, there is no d.c.-blocking capacitor in the series path to prevent d.c. currents to go in the tissue, when

https://doi.org/10.1038/s41928-023-01000-3

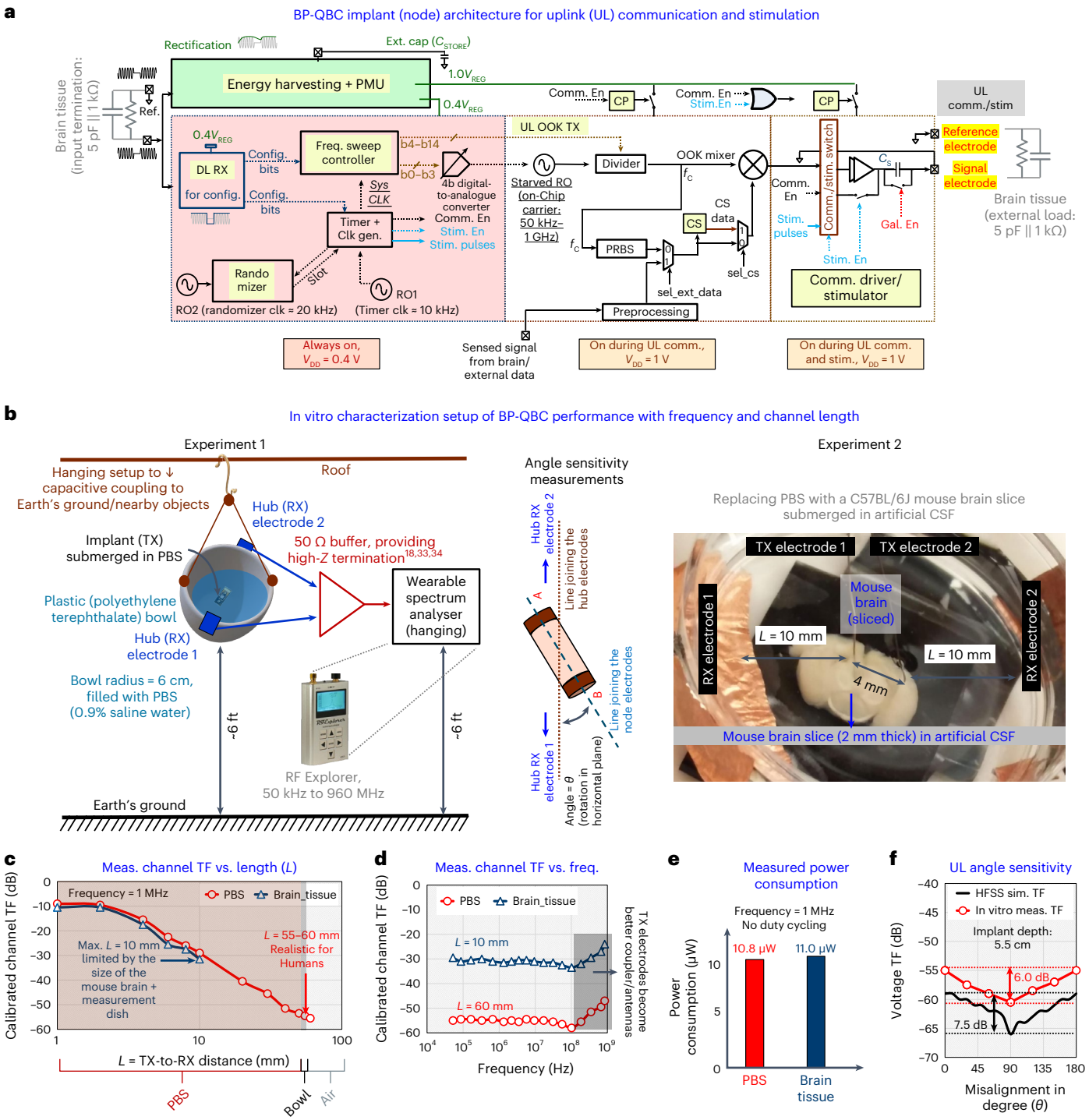

Fig. 5 | BP-QBC implant/node architecture and characterization. a, BP-QBC implant architecture for uplink communication and stimulation, containing an energy-harvesting unit and power management unit (PMU), a downlink receiver for configuring the implant, a frequency sweep controller for channel TF characterization and output frequency generation, a randomizer to transmit the data in an implant-specific randomized time slot, a CS module and a configurable communication/stimulation switch with a driver capable of G-HBC/BP-QBC transmission and stimulation. **b**, In vitro setup for characterizing the BP-QBC channel TF versus frequency and channel length, with the implant submerged in PBS. By replacing PBS with a mouse brain slice in artificial CSF, characterization on brain tissue is performed. **c**, Measurement results for channel TF versus channel length, showing reasonable correspondence between the results with PBS and brain tissue. For the mouse brain, the maximum channel length was limited to only 10 mm due to the size of the brain, whereas measurements up to 60 mm were taken in PBS, showing a channel TF of about −60 dB, matching our simulation results in HFSS. **d**, Measured channel TF versus frequency, showing a flat response in both PBS and brain tissue in the kilohertz to tens of megahertz region, consistent with the EQS approximation. At higher frequencies, the electrodes start becoming better antennas, and electromagnetic effects can reduce the loss to some extent. **e**, Power consumption in PBS and in the brain tissue for BP-QBC at 1 MHz, without any duty cycling. **f**, Alignment sensitivity of the data link during uplink communication, showing almost 6–8 decibel worst-case degradation in the channel voltage TF for in vitro measurements, when the extended line joining the implant electrodes is at a 90° angle with the line joining the hub electrodes (as shown in **b**). Panels **a**–**d** adapted from ref. 44. Image of analyzer in panel **b** from RF Explorer[52].

https://doi.org/10.1038/s41928-023-01000-3

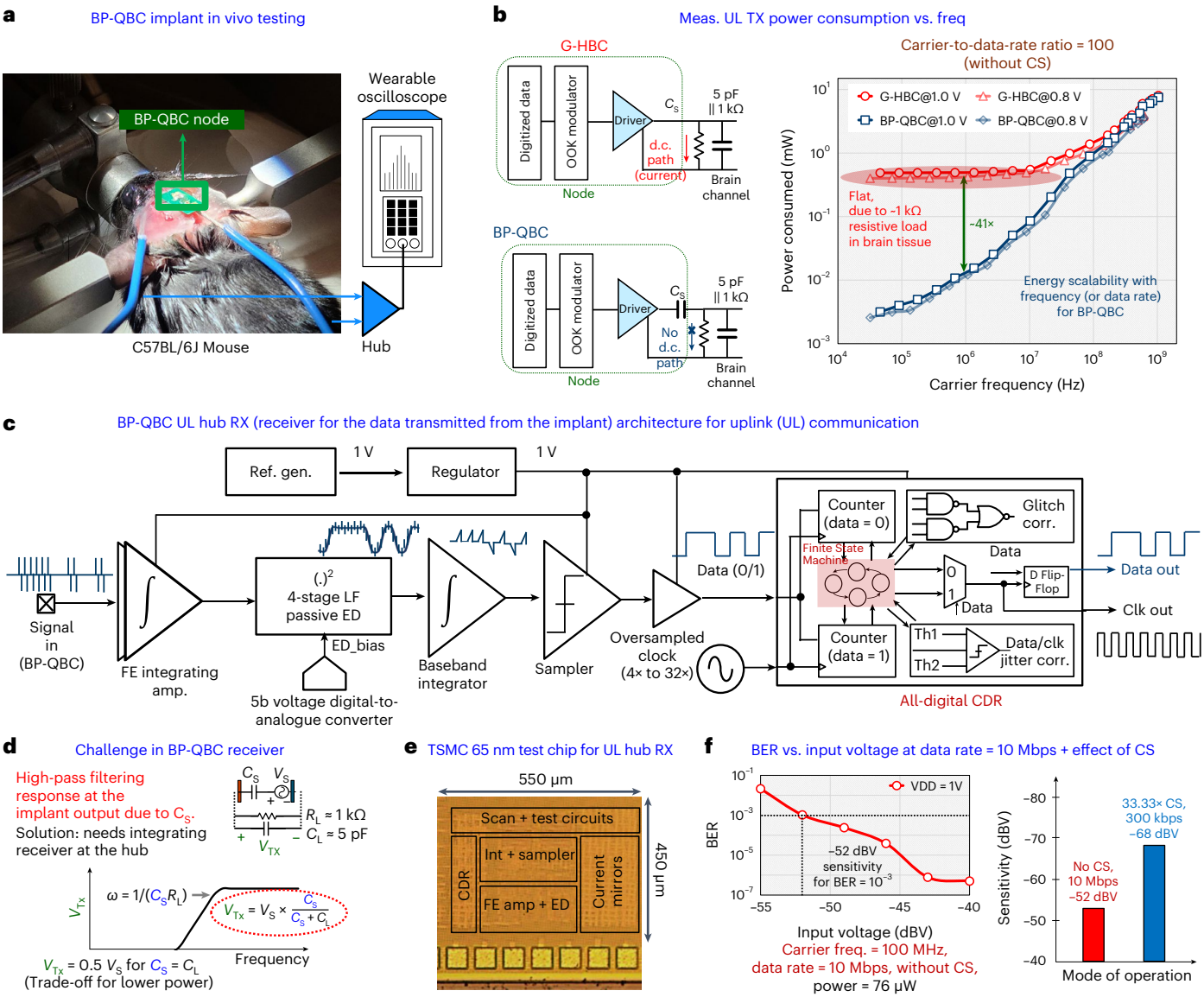

Fig. 6 | BP-QBC transmitter and receiver performances in the SoC. a, A C57BL/6J mouse, with the node placed on its brain for in vivo characterization. **b**, Comparison of uplink power consumption in G-HBC modality versus BP-QBC, demonstrating that BP-QBC is ~41× more power efficient than G-HBC at a nominal carrier frequency of 1 MHz. **c**, BP-QBC uplink receiver design at the hub, showing the integrating architecture. The FE amplifier integrates the BP-QBC inputs, which is followed by a passive envelope detector (ED) for OOK demodulation, and an integrator with a sampler that uses the clock from an oversampled clock and data recovery (CDR) circuit. **d**, Need for an integrating receiver arises to compensate for the high-pass filtering/differentiating effect introduced by the series capacitance C_S in the BP-QBC transmitter (the implant), in conjunction with the tissue load resistance R_L. **e**, A TSMC 65 nm test chip implementation for the integrating Hub RX[53] (an additional off-chip FE integrating amplifier was used for the measurement). **f**, BER versus input voltage to the hub receiver for a data rate of 10 Mbps without compression. CS can reduce the effective data rates, which will improve the sensitivity of the receiver at the same rate of information transfer. Panel **b** adapted with permission from ref. 44, IEEE.

the signal is not d.c. balanced. Since the IC generates a digital signal with on–off keying (OOK), the output is not inherently d.c. balanced, and hence, there will be a noteworthy difference in power consumption in the G-HBC and BP-QBC modes (Fig. 6b). The power consumption for G-HBC flattens out for low frequencies (<10 MHz) because of the resistive load (about 1 kΩ or lower) presented by the tissue, whereas BP-QBC power consumption continuously keeps on scaling with the frequency. At a nominal quasistatic frequency of 1 MHz, BP-QBC consumes only ~11 µW power, compared with the ~460 µW power consumption of G-HBC, thereby offering 41× lower power than G-HBC. The total power consumption in the BP-QBC transmitter was measured to be only ~0.52 µW and transmitting 1 Mbps data with 1% duty cycling, which is within the possible range of harvested power in the downlink from a wearable hub to an implant through the EQS brain channel.

Discussion on hub receiver architecture and link efficiency

A custom-made BP-QBC receiver (as part of the envisioned headphone-shaped hub) is utilized to test the bit error rate (BER) of the BP-QBC technique over data rates and input signal levels of the receiver (Fig. 6c). Figure 6d shows the primary challenge in designing such a receiver, which is the high-pass filtering or differentiating effect at the transmitter output, arising due to the d.c.-blocking capacitance. To compensate for this, the hub receiver needs to have an integrating architecture. A TSMC 65 nm IC implementation is shown in Fig. 6e,

https://doi.org/10.1038/s41928-023-01000-3

Table 1 | Comparison of BP-QBC with state-of-the-art techniques

	RF communication[6,7,13]	Inductive communication[11,12]	Optical communication[8]	Ultrasonic communication[9]	Magneto-electric communication[10]	C-HBC[36,38]	This work	
							G-HBC (reference design)	BP-QBC (focus of this work)
External components	Coil+capacitors	Coil+capacitors	LED+photovoltaic diode+electrodes	Piezo-device+electrodes	Magneto-electric film+capacitor+electrodes	Battery+electrodes	Capacitor+electrodes	**Capacitor+electrodes**
Sub-cranial repeater/relay	Yes	No	Yes	Yes	No	No	No	**No**
Node-to-hub distance	~10 mm	~10 mm	~20 mm	~50 mm	~30 mm	~10 mm	~60 mm	**~60 mm**
End-to-end channel loss (60 mm depth)	High (>80 dB)	High (>80 dB)	High (>80 dB)	High (>80 dB)	Moderate (~80 dB)	High (>80 dB)	Low (~60 dB)	**Low (~60 dB)**
Power consumption	High (>500 μW)	High (>100 μW)	Very low (<1 μW)	Low (<50 μW)	High (>500 μW)	Very low* (<5 μW)	Low* (<10 μW)	**Very low* (<1 μW @ 1 Mbps)**
Maximum data rate (bps)	Moderate (~1M)	Low (~100k)	Very low (~100)	Very low (~100)	Moderate (~1M)	High (>10M)	High (>10M)	**High (>10M)**
Energy efficiency (pJ b^{-1})	Inefficient (>500)	Inefficient (>1,000)	Inefficient (>1,000)	Inefficient (>10,000)	Inefficient (>500)	Efficient (~50)	Inefficient (>500)	**Efficient (~50)**

*Estimated with 1% duty cycling at 10 MHz carrier frequency and 1 Mbps data rate, without any data compression. Note: specifications for the proposed BP-QBC approach are presented in boldface. The state-of-the-art techniques for wireless communication in a brain implant are RF, inductive, optical, ultrasonic, magneto-electric and traditional HBC methods.

whereas the BER versus input voltage to the hub receiver for a data rate of 10 Mbps is demonstrated in Fig. 6f. This experiment is performed with a carrier frequency of 100 MHz, which is near the boundary of EQS and electromagnetic range of frequencies, as shown by the channel TF (Fig. 5d). For a target BER of 10^{-3} at 10 Mbps data rate, the required input-voltage level at the receiver for the current experiment is about −52 dBV (~2.5 mV), which means that even for a channel loss of about 50 dB, the transmit voltage level of 1 V should be sufficient for achieving a BER of $< 10^{-3}$ at a data rate of 10 Mbps. However, for higher channel losses (larger implant depth), we shall need to use lower data rates to achieve a similar BER. The data compressive sensing (CS) unit implemented in the BP-QBC node transmitter consequentially helps for such high-loss scenarios. With a 33.33× data compression, 300 kbps data rate through the channel can effectively represent the same 10 Mbps communication. The sensitivity of the receiver can then be improved from −52 dBV (no compression, 10 Mbps, 100 MHz carrier) to −68 dBV (33.33× compression, 300 kbps, 30 MHz EQS carrier) for a target BER of 10^{-3} (Fig. 6f).

Table 1 compares BP-QBC (EQS) with state-of-the-art techniques for wireless communication in a brain implant, including RF, inductive, optical, ultrasonic, magneto-electric and traditional G-HBC methods. Compared with RF, the absorption of EQS signals in the brain tissue is lower. Additionally, unlike optical or ultrasonic techniques, EQS is not affected much by the presence of the skull (which necessitates sub-cranial repeaters/relay units for optical and ultrasonic communication). This, in addition to the advantage that BP-QBC does not require any transduction of energy (unlike optical, ultrasonic or magneto-electric techniques), allows us to have only about 60 dB end-to-end channel loss as found from our analysis, simulations and measurement results. Even though the power consumption for optical and ultrasonic methods can be made extremely low, the data rates are usually limited by the sensitivity of the receiver, which depends on the backscattered signals. Conversely, HBC techniques (such as C-HBC, G-HBC and BP-QBC) allow high data rates with low power and proper duty cycling. As explained earlier, BP-QBC has a system TF similar to G-HBC, with a power consumption similar to C-HBC, thereby making it one of the most promising techniques of communication with a brain implant. It could, however, be argued that optical and ultrasonic techniques offer better spatial resolution due to the smaller wavelengths, and leads to miniaturized implants. BP-QBC, however, offers a much better end-to-end system loss, allowing room for further miniaturization compared with the implementation presented in this Article. The analysis and comparison of the end-to-end system loss for different techniques is presented in Supplementary Note 2 and Supplementary Table 1.

In addition to low power consumption, high data rates and no transduction loss, BP-QBC also promises to exhibit notable security benefits for an implant. Since the EQS signals do not radiate outside the human body to a large extent, all the EQS HBC modalities are inherently more secure than RF techniques where the signals leak outside the body and can be picked up by an attacker at a distance of a few centimetres to a few metres. Our previous works[42,45] have explored the security properties of G-HBC and C-HBC in detail, and compared them with RF techniques to show that EQS HBC techniques exhibit a private space that is ~30× better[45] than traditional radiative electromagnetic signalling, thereby making it harder for a malicious attacker to snoop in. A detailed analysis of the security properties of BP-QBC and a comparison with the security of optical, ultrasonic and magneto-electric techniques is out of the scope of the current Article and will be analysed in a future work.

Conclusions

We have reported a BP-QBC link with fully electrical quasistatic signalling for wireless communication from a brain implant. In the EQS regime, the signal wavelengths are much larger than the channel length through the body, which results in lower signal leakage, leading to better security. Additionally, because of the lower power consumption at the transmitter (due to a lower frequency of operation and the ability to have high-impedance terminations) and lower absorption in the brain tissue, the EQS technique is preferred over electromagnetic operation. Due to no field transduction requirements, the end-to-end channel loss in BP-QBC is only around 60 dB at a distance of around 55 mm with a 5 mm^3 implant, which is >20 dB better than competing (optical/ultrasound/magneto-electric) techniques, and allows room for further miniaturization of the node.

Understanding that the EQS signal transfer through the brain channel occurs through a.c. electric fields, and the primary source of power consumption is due to galvanic d.c. currents arising from the finite conductivity of brain tissues, we used a d.c.-blocking capacitor to block the d.c. paths through the brain tissue without meaningfully

affecting the biphasic a.c. communication at EQS frequencies. As a result, the power consumption in BP-QBC is around 41 times lower than traditional G-HBC at a nominal EQS frequency of 1 MHz. Furthermore, unlike optical and ultrasonic techniques, BP-QBC does not require sub-cranial interrogators/repeaters as the EQS signals can penetrate through the skull and has enough strength due to the low-loss channel. This makes BP-QBC a promising technique for high-speed, low-loss data transfer through the brain tissue within harvested energy limits.

Methods

This section provides details related to our simulation and experimental methods, to facilitate reproduction of the results by another independent researcher.

Setup for FEM simulation

Simulator and models. All the EQS simulations have been performed in Ansys HFSS, which is an FEM-based solver for Maxwell's equations. A detailed human head model consisting of realistic tissues (white matter + grey matter + CSF + skull + blood + skin) is used to validate the theoretical channel TF, which is taken from NEVA Electromagnetics[46]. Dielectric properties of the brain tissues have been obtained from the Gabriel-Gabriel Model[21,22].

Implant model. A simple cylindrical model made of rubber, along with two spherical copper electrodes, is used as the implant (Supplementary Fig. 1). The nominal radius of this rubber cylinder is 0.5 mm, whereas the nominal height is 4.0 mm. Two spherical copper electrodes of radius 0.5 mm are placed on the two sides of this model to represent the transmit electrodes in the node. The rubber cylinder is curved at the sides to support the two electrodes and cover them in a hemispherical manner. This implant model is floated 6 cm within the human head/brain model, whereas the head model itself is floated 1.7 m above a plane with a perfect e-boundary in HFSS, which replicates an infinite ground plane similar to Earth's ground. The excitation for the simulation is provided through differential/galvanic coupling, as described in the next sub-section.

Excitation. A differential/galvanic coupling model is used to provide excitation to the brain tissue surrounding the implant. The coupler consists of two copper spheres with a radius of 0.5 mm. The separation between the two spheres (which is filled with the rubber cylinder, curved near the electrodes) can be varied, as well as the radius of the spheres and the cylinder. A voltage source excitation is placed between the two spheres. In HFSS, this imparts an alternating potential difference with an amplitude of 1 V between the two electrodes, replicating an ideal a.c. voltage source. This is unlike the traditional lumped port excitation method in HFSS, which is suitable for 50 Ω matched excitations, but may result in unexpected reflections when coupled with a non-standard termination model.

Measurement of voltage at the hub receiver. The receiving node structure uses parallel discs of similar dimensions, placed on two sides of the head model (Fig. 3d). A lumped *RLC* boundary is placed between the electrode and ground plate at the receiver, which is set to 10 pF for capacitive high-impedance termination, modelling the capacitance between the electrode and local ground reference. The potential difference between the discs is calculated by performing a line integration of the electric field along the straight line between the extended receiving electrode plates, and ensuring that the line does not go through or near the transmitter so as to affect the integrated voltage value.

Measurement of power at the node receiver. For downlink powering purposes, the hub becomes the power transmitter and the implant becomes the power receiver. The input impedance at the implant needs to be matched with the tissue impedance for maximum power transfer. A 40 MHz differential voltage source excitation is placed between the two hub electrodes, imparting an alternating potential difference of amplitude 1 V between the two electrodes, replicating an ideal a.c. voltage source. A lumped *RLC* boundary is placed between the electrodes of the implant, which is varied from $R = 100\ \Omega$ to $R = 10\ \text{k}\Omega$. The peak potential difference (V) between the plates is calculated by integrating the electric field along a straight line between the electrode and ground plates, and the power received is calculated by the formula $P = V^2/2R$. For an a.c. amplitude of 1 V between the two electrodes at the hub, the effective r.m.s. current density at the downlink power transmitter electrodes is calculated to be $\frac{1\text{V}}{\sqrt{2}} \times \frac{1}{R_{\text{Tissue}}} \times \frac{1}{\pi r_{\text{e,C}}^2}$, where R_{Tissue} is the effective tissue impedance seen by the power transmitter (~1 kΩ), and $r_{\text{e,C}}$ is the radius of the electrodes in the power transmitter/hub (~1.3 cm for an electrode area of 4 cm^2). This results in an effective current density of 0.133 mA cm^{-2}, whereas the power transmitted becomes $\frac{1\text{V}^2}{2} \times \frac{1}{R_{\text{Tissue}}} \approx 500\ \mu\text{W}$. Using HFSS, FEM simulations are performed for worst-case channel power TF, which is found to be about −55 dB for a maximally misaligned node at a depth of about 5.5 cm, at a 90° angle with the line joining the hub electrodes (Supplementary Note 3 and Supplementary Fig. 2 provide more analysis on the misalignment). The power delivered to the 1 kΩ input impedance at the implant will be only 1.6 nW, taking into account the power division between the tissue and the implant's input impedance. However, according to the ICNIRP safety guidelines[14] (see table 4 in ref. 14), the allowable current density for the human head in occupational scenarios is f/100 mA m^{-2} for frequencies up to 10 MHz, where f denotes the frequency. This results in a maximum allowable current density of f/1M mA cm^{-2}, which is 10 mA cm^{-2} at 10 MHz. By linearly scaling this to 40 MHz (which is also the human-body-powering frequency used in previous works[35,37]), the allowable current density can be calculated to be 40 mA cm^{-2}. If we use one-fifth of this current density magnitude (8 mA cm^{-2}, which is also the limit for general public exposure), the power available at the 1 kΩ input impedance at the implant will be $1.6 \times \left(\frac{8}{0.133}\right)^2$ nW ≈ 5.8 μW, whereas the transmitted power is $500 \times \left(\frac{8}{0.133}\right)^2$ μW ≈ 1.8 W. The specific absorption rate will be much lower in the tissue, and as the Federal Communications Commission allows a specific absorption rate of 1.6 W kg^{-1} for 1 g of tissue[47], this will be within acceptable limits (please note that the human brain weighs about 1.2–1.4 kg). With an assumption that only 40–60% of the equivalent energy can be stored at the node, we estimate that only ~2.5–4.0 μW of power can be harvested at the brain implant, which is considered as the target power budget of the implant. The power transfer efficiency from the hub to the input impedance at the implant is, thus, ~5.8 μW/1.8 W ≈ 0.0003% in the worst case. However, when the node is aligned with the hub electrodes, the channel power TF is about −43 dB at an implant depth of 5.5 cm, which will lead to a best-case power transfer efficiency of ~0.005%, and in that case, the transmit power from the hub needs to be only about 200 mW for 10 μW available power at the node.

Setup for characterization experiments (in vitro/in vivo)

Node design (data transmitter and power receiver). The specifications of the implant/node for characterization experiments demanded a signal generator of a small form factor (millimetre scale or lower) with proper ground isolation, which runs on a self-sustained energy source (battery/storage capacitor), and sweeps through a few kilohertz to 1 GHz. For this purpose, an IC was built on a 1.0 mm × 1.0 mm × 0.3 mm system on a chip (SoC) fabricated in TSMC 65 nm complementary metal–oxide–semiconductor technology, which serves as an ultralow-power implantable signal generator. The implemented BP-QBC SoC (Fig. 5a) is equipped with (1) a 52 pJ b^{-1} energy–frequency-scalable uplink transmitter with an on-chip clock, OOK-based modulation and variable duty cycling, along with CS for data volume reduction, and collision avoidance and sending data from

multiple implants; (2) an always-on 31 nW downlink receiver to obtain system configuration bits and control signals from the wearable hub; (3) a biphasic stimulator with 89.2% current efficiency ($I_{Stim}/I_{d.c.}$ = ratio of current supplied for stimulation with the consumed d.c. current); and (4) an energy harvester utilizing a 30-stage RF rectifier[48] that can generate a 1 V supply for the SoC with only about 70 mV_p receiver input in the downlink. Two different supply domains are implemented: a 0.4 V domain for low-leakage/low-power always-on timer/controller modules and a separate 1 V domain for duty-cycled data communication and stimulation. The power management unit in the SoC consists of a 13 nW reference voltage generator (for both 0.4 V and 1.0 V supplies) and two 24 nW low-dropout regulators that generate V_{DD} for the SoC, utilizing the energy harvested from the 30-stage RF rectifier. In the current implementation, the SoC utilizes 1:100 duty cycling with a 100-ms-long transmit phase, and a 100-ms-long stimulation phase within a total time of 10 s by default. Using the downlink control signals, additional modes with 1:1,000 and 1:10 duty cycling can also be configured, or duty cycling can be turned off. Figure 5a presents a simplified diagram of the building blocks of the SoC. The external energy storage capacitor (C_{STORE}) at the output of the RF rectifier is carefully optimized during design time for a maximum data rate of 10 Mbps with a charging time of ≪100 s and a voltage drop of ≪100 mV during each of the transmit and stimulation phases. A 17 nW charge pump generates an output voltage ($V_{PUMP} \approx 1.8$ V), which is much higher than V_{DD} (1 V), and is utilized to bias specific power gates on the supply of the duty-cycled modules in deep subthreshold during the off state to reduce their leakage. Using such bootstrapping techniques, the leakage at the power gates is reduced from 0.51 µW to about 1 nW (>500× reduction). The average power consumption in the SoC is only 1.15 µW (including leakage) with 1% duty cycling, out of which 0.52 µW is consumed for BP-QBC, at a 3 MHz carrier frequency (1 Mbps effective data rate with 33.33× compression). A wake-up-controller-based CS front end (FE) allows the compression of any acquired data in the neural sensor to reduce the overall transmit data rates. The CS module consists of an on-chip two-stage discrete-wavelet-transform-based optional sparsifier and a dual varying-seed pseudo-random-bit-sequence-based sensing-matrix generator, and allows a variable compression factor between 5.00× and 33.33×. A ring-oscillator-based physical unclonable function designed as a nine-bit pseudo-random bit sequence generator is utilized to specify randomized time slots for transmission and stimulation in different nodes within the brain. This enables an inherent collision avoidance scheme without any complex medium access control implementation. The downlink receiver in the implant SoC consists of a 10.1 nW FE amplifier, a 3.2 nW four-stage passive envelope detector for the demodulation of configuration bits and a 16.2 nW fully digital oversampled clock and data recovery circuit for data decoding. Further details on the implementation can be found in our recent works[44,49].

Design of the uplink hub receiver. A custom-made BP-QBC receiver (as part of the headphone-shaped hub) is utilized to test the BER of the BP-QBC technique over data rates and input signal levels of the receiver (Fig. 6c). This is implemented in the form of an integrating receiver on a a separate IC, as part of the BP-QBC uplink architecture in the hub. An FE integrating amplifier integrates the BP-QBC inputs, which is followed by a passive envelope detector for OOK demodulation, and an integrator followed by a sampler that uses the clock from an oversampled clock and data recovery unit. The need for an integrating receiver arises to compensate for the high-pass filtering/differentiating effect introduced by the series capacitance C_S in the BP-QBC transmitter (the implant), in conjunction with the tissue load resistance R_L (Fig. 6b,d). The TSMC 65 nm ASIC implementation is shown in Fig. 6e.

CS in the implant. Since neural signals can range from very low-frequency (few millihertz to tens of hertz) local field potentials to higher-frequency (tens of hertz to a few kilohertz) action potentials, the data rates for a single channel can reach a few hundreds of kilobits per second. As an example, a signal acquisition module with 10 kHz bandwidth, 5× oversampling and 16 bits per sample results in a data rate of 10k × 5 × 16 = 800 kbps. For multichannel signal acquisition, this requirement increases further. If a true carrier-to-data-rate ratio of 100 is utilized for data transfer using OOK modulation, the power consumption becomes ~770 µW for BP-QBC and ~1,120 µW for G-HBC (Fig. 6b), requiring aggressive duty cycling for communicating within the available power limit (<4 µW) at the implant (Fig. 3d,e). On the other hand, a CS FE can reduce the overall energy consumption per bit by ~16× and reducing the data rate (and hence the required carrier frequency) by 33×, as shown in our earlier works[44,49]. This results in an effective carrier-to-data-rate ratio of ~3, reducing the power consumption of BP-QBC to only ~26 µW for 800 kbps (at 2.4 MHz) transmission. With a 10 MHz carrier, the energy efficiency of the BP-QBC system is 835 pJ b^{-1} without CS (with a carrier-to-data-rate ratio of 100), which reduces to only 52 pJ b^{-1} with CS. If a true carrier-to-data-rate ratio of around 10 is allowed for the proper detection of data at the receiver, the energy efficiency with CS can reduce to <10 pJ b^{-1}. At 1 Mbps data rate with CS (compression factor of 33.33×), the power consumption in the BP-QBC driver is only 0.52 µW with 1% duty cycling, which is within the range of available power (<4 µW) at the implant using power transmission through the brain tissue.

Collision avoidance in implants. As mentioned earlier, another important feature in the SoC is an inherent collision avoidance scheme implemented to avoid/reduce the chances of multiple nodes transmitting data at the same time (or stimulating at the same time) within the brain. Due to the small amount of available power and the high bandwidth requirement of neural signals, multiple nodes cannot simultaneously operate with frequency-division multiplexing, and hence, time-division multiplexing needs to be used. To ensure that time-division multiplexing can be implemented (1) without any medium access control layer protocol and (2) without any synchronization among multiple nodes placed within the brain, a physical-unclonable-function-based communication and stimulation slot selector is utilized in conjunction with duty cycling. Theoretically, 1% duty cycling allows 100 implants to simultaneously operate, whereas a nine-bit ring-oscillator-based physical unclonable function ensures that there needs to be at least 27 nodes operating simultaneously so that at least two of the nodes transmit at the same time slot with 50% (or more) probability, which can be proven from theory[50].

Setup for in vitro experiments. Figure 5b demonstrates the measurement setup and methods for characterizing the in vitro BP-QBC channel TF as a function of frequency as well as the implant-to-hub distance. The 1.0 mm × 1.0 mm × 0.3 mm SoC is housed on a flexible polyimide PCB of dimensions 4.4 mm × 2.4 mm, and is subsequently submerged in PBS water placed in a hemispherical plastic (polyethylene terephthalate) bowl of 60 mm radius, which has similar dimensions as that of the human skull. The entire setup is suspended from the roof to minimize any parasitic capacitive coupling to Earth's ground and nearby objects, thereby improving ground isolation during the measurements. Two differential metal electrodes attached to the sides of the bowl work as the receiving electrodes, which are connected to a TI BUF602 buffer configured as a 50 Ω driver for measurement instruments. The TI buffer offers about 2 pF capacitive termination at the input of the receiver, which helps in establishing a wideband HBC channel as shown in earlier works[18,31,33,34]. On the other hand, a traditional 50 Ω termination would have resulted in a high-pass channel. The output of the buffer is terminated with 50 Ω, and goes to a handheld spectrum analyser from RF Explorer. The IC sweeps through different configurable frequencies in the range of 40 kHz to 1 GHz to characterize the BP-QBC signal transmission as a function of frequency. For characterizing the channel TF as a function of the implant-to-hub distance, the receiving

electrodes are placed inside the bowl, and are subsequently moved at different distances from the implant. The experiments are repeated with brain slices from a C57BL/6J mouse strain, adhering to the guidelines of the overseeing Institutional Animal Care and Use Committee at Purdue University. During this experiment, 500-µm- to 2-mm-thick slices are placed in a measurement dish containing artificial CSF saturated with carbogen (95% O_2 + 5% CO_2). Two differential electrodes from the transmitter are placed on the surface of the brain slices for excitation. The receiving electrodes are placed at different distances from the brain slices for this experiment. A total of seven instances of the IC were tested, and the nominal results were reported. During the in vitro experiments, the implant is powered from a precharged 2.00 mm × 1.25 mm × 0.85 mm capacitor, which is housed on the back side of the flexible polyimide PCB.

Setup for in vivo experiments. Figure 6a exhibits the setup and methods for demonstrating BP-QBC signal transfer and measure the power consumption of the device. The 1.0 mm × 1.0 mm × 0.3 mm SoC is housed on a flexible polyimide PCB of dimensions 4.4 mm × 2.4 mm, and is placed on the brain of a live C57BL/6J mouse. All the research protocols were approved and monitored by the Institutional Animal Care and Use Committee at Purdue University, and all the research was performed in accordance with relevant National Institutes of Health guidelines and regulations. The mouse was anaesthetized with 2–3% isoflurane throughout the surgery. After shaving the hair, the animal was fixed on a stereotaxic frame so that the head does not move during the experiment, and the head skin was sterilized. Up to 2.5 cm sagittal incision was made in the skin over the skull, and a bilateral craniotomy was performed using a precision surgery dental drill. After the craniotomy, the skull in the midline was thinned down to improve contact with the BP-QBC implant. The insertion of the BP-QBC electrodes was manually done. Two differential electrodes placed on the sides of the skull work as the receiving electrodes, and were fixed with super glue to keep them in place. The receiving electrodes were connected to a TI BUF602 buffer configured as a 50 Ω driver, with about 2 pF capacitive termination at the input side. The output of the buffer goes to a handheld oscilloscope from RF Explorer with 50 Ω termination. During the in vivo experiments, the implant is powered from a precharged 2.00 mm × 1.25 mm × 0.85 mm capacitor, which is housed on the back side of the flexible polyimide PCB. However, for power consumption measurements, the implant is connected to a d.c. power supply using thin copper wires.

Reporting summary

Further information on research design is available in the Nature Portfolio Reporting Summary linked to this article.

Data availability

The data that support the plots within this paper and other findings of this study are available via GitHub at https://github.com/WISE-Lab-UF/NatE23_BP-QBC. Further details can be obtained from the corresponding authors upon reasonable request. Source data are provided with this paper.

Code availability

Custom codes used to process the data are available via GitHub at https://github.com/WISE-Lab-UF/NatE23_BP-QBC. Further details can be obtained from the corresponding authors upon reasonable request.

References

1. Chen, Z., Xi, J., Huang, W. & Yuen, M. F. Stretchable conductive elastomer for wireless wearable communication applications. *Sci. Rep.* **7**, 10958 (2017).
2. Huang, X. et al. Highly flexible and conductive printed graphene for wireless wearable communications applications. *Sci. Rep.* **5**, 18298 (2015).
3. Rabaey, J. M. The human intranet—where swarms and humans meet. *IEEE Pervasive Comput.* **14**, 78–83 (2015).
4. Hessar, M., Iyer, V. & Gollakota, S. Enabling on-body transmissions with commodity devices. In *Proc. 2016 ACM International Joint Conference on Pervasive and Ubiquitous Computing* 1100–1111 (ACM, 2016).
5. *Interfacing with the Brain* (accessed 25 December 2021); https://neuralink.com/approach/
6. Lee, J. et al. Neural recording and stimulation using wireless networks of microimplants. *Nat. Electron.* **4**, 604–614 (2021).
7. Borton, D. et al. An implantable wireless neural interface for recording cortical circuit dynamics in moving primates. *J. Neural Eng.* **10**, 026010 (2013).
8. Lim, J. et al. A 0.19×0.17mm^2 wireless neural recording IC for motor prediction with near-infrared-based power and data telemetry. In *Proc. 2020 IEEE International Solid-State Circuits Conference (ISSCC) Digest of Technical Papers* (ed Fujino, L. C.) **63**, 416–418 (IEEE, 2020).
9. Ghanbari, M. et al. A 0.8mm^3 ultrasonic implantable wireless neural recording system with linear AM backscattering. In *Proc. 2019 IEEE International Solid-State Circuits Conference (ISSCC) Digest of Technical Papers* (ed Fujino, L. C.) **62**, 284–286 (IEEE, 2019).
10. Yu, Z. et al. An 8.2 mm^3 implantable neurostimulator with magnetoelectric power and data transfer. In *Proc. 2020 IEEE International Solid-State Circuits Conference (ISSCC) Digest of Technical Papers* (ed Fujino, L. C.) **63**, 510–512 (IEEE, 2020).
11. Jia, Y. et al. A mm-sized free-floating wirelessly powered implantable optical stimulating system-on-a-chip. In *Proc. 2018 IEEE International Solid-State Circuits Conference (ISSCC) Digest of Technical Papers* (ed Fujino, L. C.) **61**, 468–470 (IEEE, 2018).
12. Lo, Y. et al. A 176-channel 0.5cm^3 0.7 g wireless implant for motor function recovery after spinal cord injury. In *Proc. 2016 IEEE International Solid-State Circuits Conference (ISSCC) Digest of Technical Papers* (ed Fujino, L. C.) **59**, 382–383 (IEEE, 2016).
13. Lee, J. et al. An implantable wireless network of distributed microscale sensors for neural applications. In *Proc. 2019 International IEEE/EMBS Conference on Neural Engineering (NER)* 871–874 (IEEE, 2019).
14. *ICNIRP Guidelines for Limiting Exposure to Time-Varying Electric, Magnetic and Electromagnetic Fields* (accessed 5 Feb 2022); https://www.icnirp.org/cms/upload/publications/ICNIRPemfgdl.pdf
15. IEEE standard for safety levels with respect to human exposure to radio frequency electromagnetic fields, 3 kHz to 300 GHz. In *IEEE Std C95.1-2005 (Revision of IEEE Std C95.1-1991)* 1–238 (IEEE, 2006).
16. IEEE standard for safety levels with respect to human exposure to electromagnetic fields, 0-3 kHz. In *IEEE Std C95.6-2002* 1–64 (IEEE, 2002).
17. Modak, N., Nath, M., Chatterjee, B., Maity, S. & Sen, S. Bio-physical modeling of galvanic human body communication in electro-quasistatic regime. *IEEE Trans. on Biomed. Eng.* **69**, 3717–3727 (2022).
18. Datta, A., Nath, M., Yang, D. & Sen, S. Advanced bio-physical model to capture channel variability for EQS capacitive HBC. *IEEE Trans. Biomed. Eng.* **68**, 3435–3446 (2021).
19. *Lecture Notes|Electromagnetic Energy: From Motors to Lasers|Electrical Engineering and Computer Science|MIT OpenCourseWare* (accessed 15 March 2021); https://ocw.mit.edu/courses/electrical-engineering-and-computer-science/6-007-electromagnetic-energy-from-motors-to-lasers-spring-2011/lecture-notes/
20. Larsson, J. Electromagnetics from a quasistatic perspective. *Am. J. Phys.* **75**, 230–239 (2007).

21. *Tissue Properties* (accessed 25 December 2021); https://itis.swiss/virtual-population/tissue-properties/database/dielectric-properties/
22. Gabriel, S., Lau, R. W. & Gabriel, C. The dielectric properties of biological tissues: III. Parametric models for the dielectric spectrum of tissues. *Phys. Med. Biol.* **41**, 2271 (1996).
23. Zimmerman, T. G. Personal area networks: near-field intrabody communication. *IBM Syst. J.* **35**, 609–617 (1996).
24. Oberle, M. *Low Power Systems-on-Chip for Biomedical Applications*. PhD thesis, ETH Zurich (2002).
25. Hachisuka, K. et al. Development of wearable intra-body communication devices. *Sens. Actuators Phys.* **105**, 109–115 (2003).
26. Cho, N. et al. The human body characteristics as a signal transmission medium for intrabody communication. *IEEE Trans. Microw. Theory Tech.* **55**, 1080–1086 (2007).
27. Yanagida, T. Human body communication system and communication device. US patent 7664476B2 (2010).
28. Xu, R., Zhu, H. & Yuan, J. Electric-field intrabody communication channel modeling with finite-element method. *IEEE Trans. Biomed. Eng.* **58**, 705–712 (2011).
29. Lucev, Ž., Krois, I. & Cifrek, M. A capacitive intrabody communication channel from 100 kHz to 100 MHz. *IEEE Trans. Instrum. Meas.* **61**, 3280–3289 (2012).
30. Bae, J., Cho, H., Song, K., Lee, H. & Yoo, H. The signal transmission mechanism on the surface of human body for body channel communication. *IEEE Trans. Microw. Theory Tech.* **60**, 582–593 (2012).
31. Park, J., Garudadri, H. & Mercier, P. P. Channel modeling of miniaturized battery-powered capacitive human body communication systems. *IEEE Trans. Biomed. Eng.* **64**, 452–462 (2017).
32. Cho, H. et al. A 79 pJ/b 80 Mb/s full-duplex transceiver and a 42.5 μW 100 kb/s super-regenerative transceiver for body channel communication. *IEEE J. Solid-State Circuits* **51**, 310–317 (2016).
33. Maity, S., Chatterjee, B., Chang, G. & Sen, S. Bodywire: a 6.3pJ/b 30Mb/s –30dB SIR-tolerant broadband interference-robust human body communication transceiver using time domain interference rejection. *IEEE J. Solid-State Circuits* **54**, 2892–2906 (2019).
34. Maity, S. et al. Bio-physical modeling, characterization, and optimization of electro-quasistatic human body communication. *IEEE Trans. Biomed. Eng.* **66**, 1791–1802 (2019).
35. Li, J. et al. Human-body-coupled power-delivery and ambient-energy-harvesting ICs for a full-body-area power sustainability. In *Proc. IEEE International Solid-State Circuits Conference (ISSCC) Digest of Technical Papers* (ed Fujino, L. C.) **63**, 514–515 (IEEE, 2020).
36. Yuk, B. et al. An implantable body channel communication system with 3.7-pJ/b reception and 34-pJ/b transmission efficiencies. *IEEE Solid-State Circuits Lett.* **3**, 50–53 (2020).
37. Li, J. et al. Body-coupled power transmission and energy harvesting. *Nat. Electron.* **4**, 530–538 (2021).
38. Lee, C. et al. A miniaturized wireless neural implant with body-coupled data transmission and power delivery for freely behaving animals. In *Proc. 2022 IEEE International Solid-State Circuits Conference (ISSCC) Digest of Technical Papers* (ed Fujino, L. C.) **65**, 1–3 (IEEE, 2022).
39. Chatterjee, B. et al. A 65 nm 63.3 μW 15 Mbps transceiver with switched-capacitor adiabatic signaling and combinatorial-pulse-position modulation for body-worn video-sensing AR nodes. In *Proc. 2022 IEEE International Solid-State Circuits Conference (ISSCC) Digest of Technical Papers* (ed Fujino, L. C.) **65**, 276–278 (IEEE, 2022).
40. Wegmueller, M. S., Oberle, M., Felber, N., Kuster, N. & Fichtner, W. Signal transmission by galvanic coupling through the human body. *IEEE Trans. Instrum. Meas.* **59**, 963–969 (2010).
41. Callejón, M. A., Naranjo-Hernández, D., Reina-Tosina, J. & Roa, L. M. A. Comprehensive study into intrabody communication measurements. *IEEE Trans. Instrum. Meas.* **62**, 2446–2455 (2013).
42. Datta, A. et al. A quantitative analysis of physical security and path loss with frequency for IBOB channels. *IEEE Microw. Wireless Compon. Lett.* **32**, 792–795 (2022).
43. Zhao, Z. et al. Ionic communication for implantable bioelectronics. *Sci. Adv.* **8**, 50–53 (2022).
44. Chatterjee, B. et al. A 1.15μW 5.54mm^3 implant with a bidirectional neural sensor and stimulator SoC utilizing bi-phasic quasistatic brain communication achieving 6kbps-10Mbps uplink with compressive sensing and RO-PUF based collision avoidance. In *Proc. 2021 IEEE Symposium on VLSI Circuits* 1–2 (IEEE, 2021).
45. Das, D., Maity, S., Chatterjee, B. & Sen, S. Enabling covert body area network using electro-quasistatic human body communication. *Sci. Rep.* **9**, 4160 (2019).
46. *NEVA Electromagnetics* (accessed 5 February 2022); https://www.nevaelectromagnetics.com/
47. *Specific Absorption Rate (SAR)* (accessed 17 June 2023); https://www.fcc.gov/general/specific-absorption-rate-sar-cellular-telephones#:~:text=The%20FCC%20limit%20for%20public
48. Roberts, N. et al. A 236nW –56.5dBm-sensitivity Bluetooth low-energy wakeup receiver with energy harvesting in 65nm CMOS. In *Proc. 2016 IEEE International Solid-State Circuits Conference (ISSCC) Digest of Technical Papers* (ed Fujino, L. C.) **59**, 382–383 (IEEE, 2016).
49. Kumar, G. K., Chatterjee, B & Sen, S. CS-Audio: A 16 pJ/b 0.1-15Mbps compressive sensing IC with DWT sparsifier for audio-AR. *IEEE J. Solid-State Circuits* **57**, 2220–2235 (2022).
50. Sen, O. & Chatterjee, B. Modified ring-oscillator physical unclonable function (RO-PUF) based PRBS generation as a device signature in distributed brain implants. In *Proc. 2023 IEEE International Midwest Symposium on Circuits and Systems (MWSCAS)* in press (IEEE, 2023).
51. *MakeHuman|Open Source Tool for Making 3D Characters* (accessed 26 April 2022); http://www.makehuman.org/license.php
52. *RF Explorer* (accessed 17 June 2023); http://j3.rf-explorer.com/
53. Maity, S. et al. Sub-μWRComm: 415-nW 1–10-kb/s physically and mathematically secure electro-quasi-static HBC node for authentication and medical applications. *IEEE J. Solid-State Circuits* **56**, 788–802 (2021).

Acknowledgements

This work was supported by the Air Force Office of Scientific Research YIP Award (FA9550-17-1-0450, to S.S.), the National Science Foundation CAREER Award (grant no. 1944602, to S.S.) and the National Science Foundation CRII Award (CNS 1657455, to S.S.). We would like to thank D. Das (Purdue University) and N. Modak (Purdue University) for their co-operation and support during the development of the ICs for the neural node. The experiments in K.J. lab were supported by a Purdue Institute for Integrative Neuroscience seed grant.

Author contributions

B.C. and S.S. conceived the idea. B.C., S.S. and M.N. contributed to the design of the experiments for BP-QBC. B.C., M.N., G.K.K. and S.S. conducted the theoretical analysis, numerical simulations and node design, as well as performed the characterization experiments. B.C., S.X., K.J. and G.K.K. performed the in vitro and in vivo animal experiments. B.C., S.S., M.N. and K.J. analysed the experimental data. B.C., M.N. and S.S. wrote the paper. All the authors contributed to reviewing and revising the manuscript.

Competing interests
The authors declare no competing interests.

Additional information
Supplementary information The online version contains supplementary material available at https://doi.org/10.1038/s41928-023-01000-3.

Correspondence and requests for materials should be addressed to Baibhab Chatterjee or Shreyas Sen.

Peer review information *Nature Electronics* thanks Cong Ding and the other, anonymous, reviewer(s) for their contribution to the peer review of this work.

nature portfolio

Corresponding author(s): Baibhab Chatterjee (bchatte@purdue.edu), Shreyas Sen (shreyas@purdue.edu)

Last updated by author(s): Jun 25, 2023

Reporting Summary

Nature Portfolio wishes to improve the reproducibility of the work that we publish. This form provides structure for consistency and transparency in reporting. For further information on Nature Portfolio policies, see our Editorial Policies and the Editorial Policy Checklist.

Statistics

For all statistical analyses, confirm that the following items are present in the figure legend, table legend, main text, or Methods section.

n/a	Confirmed	
☐	☒	The exact sample size (*n*) for each experimental group/condition, given as a discrete number and unit of measurement
☐	☒	A statement on whether measurements were taken from distinct samples or whether the same sample was measured repeatedly
☒	☐	The statistical test(s) used AND whether they are one- or two-sided *Only common tests should be described solely by name; describe more complex techniques in the Methods section.*
☒	☐	A description of all covariates tested
☒	☐	A description of any assumptions or corrections, such as tests of normality and adjustment for multiple comparisons
☒	☐	A full description of the statistical parameters including central tendency (e.g. means) or other basic estimates (e.g. regression coefficient) AND variation (e.g. standard deviation) or associated estimates of uncertainty (e.g. confidence intervals)
☒	☐	For null hypothesis testing, the test statistic (e.g. *F*, *t*, *r*) with confidence intervals, effect sizes, degrees of freedom and *P* value noted *Give P values as exact values whenever suitable.*
☒	☐	For Bayesian analysis, information on the choice of priors and Markov chain Monte Carlo settings
☒	☐	For hierarchical and complex designs, identification of the appropriate level for tests and full reporting of outcomes
☒	☐	Estimates of effect sizes (e.g. Cohen's *d*, Pearson's *r*), indicating how they were calculated

Our web collection on statistics for biologists contains articles on many of the points above.

Software and code

Policy information about availability of computer code

Data collection	For this research, the following software/tools were used to collect data, design integrated circuits and program measurement devices: MATLAB (version R2019b), HFSS (Ansys, version 2020, version 2022 R1), Cadence Virtuoso (IC6.1.8-64b)
Data analysis	No custom data analysis was performed. he plots were generated with MATLAB (version R2019b) and Microsoft Excel (version 2019)

For manuscripts utilizing custom algorithms or software that are central to the research but not yet described in published literature, software must be made available to editors and reviewers. We strongly encourage code deposition in a community repository (e.g. GitHub). See the Nature Portfolio guidelines for submitting code & software for further information.

Data

Policy information about availability of data

All manuscripts must include a data availability statement. This statement should provide the following information, where applicable:

- Accession codes, unique identifiers, or web links for publicly available datasets
- A description of any restrictions on data availability
- For clinical datasets or third party data, please ensure that the statement adheres to our policy

The authors declare that [the/all other] data supporting the findings of this study are available within the paper, its supplementary information files and the github link: https://github.com/WISE-Lab-UF/NatE23_BP-QBC. Any other details on the tabulated data for the plots within this paper are available from the corresponding author upon request.

Research involving human participants, their data, or biological material

Policy information about studies with human participants or human data. See also policy information about sex, gender (identity/presentation), and sexual orientation and race, ethnicity and racism.

Reporting on sex and gender	N/A. No human studies were performed.
Reporting on race, ethnicity, or other socially relevant groupings	N/A. No human studies were performed.
Population characteristics	N/A. No human studies were performed.
Recruitment	N/A. No human studies were performed.
Ethics oversight	N/A. No human studies were performed.

Note that full information on the approval of the study protocol must also be provided in the manuscript.

Field-specific reporting

Please select the one below that is the best fit for your research. If you are not sure, read the appropriate sections before making your selection.

☒ Life sciences ☐ Behavioural & social sciences ☐ Ecological, evolutionary & environmental sciences

For a reference copy of the document with all sections, see nature.com/documents/nr-reporting-summary-flat.pdf

Life sciences study design

All studies must disclose on these points even when the disclosure is negative.

Sample size	The sample size was chosen considering that the major focus of this study is in the validation of only the BP-QBC signal transfer analysis, and hence large number of biological samples/animals were not used. The in-vitro and in-vivo measurements were done one one animal each. The data was collected from 7 instances of the integrated circuit (IC), and was plotted for the nominal and repeatable scenarios.
Data exclusions	The data was collected from 7 instances of the integrated circuit (IC), and was plotted for the nominal and repeatable scenarios. Non-repeatable measurements were excluded.
Replication	The experiments have been performed in phosphate buffered saline (PBS - a proxy for the brain tissue + CSF environment) or with the animal tissue independently, and the replication of the results was successful. Multiple ICs were tested for the in-vitro studies. In-vivo experiment with one animal confirmed similar results as found during in-vitro studies.
Randomization	This study focuses on the scientific and hardware system validation of BP-QBC and no randomization studies were needed and/or performed.
Blinding	This study focuses on the scientific and hardware system validation of BP-QBC and no blinding studies were needed and/or performed.

Reporting for specific materials, systems and methods

We require information from authors about some types of materials, experimental systems and methods used in many studies. Here, indicate whether each material, system or method listed is relevant to your study. If you are not sure if a list item applies to your research, read the appropriate section before selecting a response.

Materials & experimental systems

n/a	Involved in the study
☒	☐ Antibodies
☒	☐ Eukaryotic cell lines
☒	☐ Palaeontology and archaeology
☐	☒ Animals and other organisms
☒	☐ Clinical data
☒	☐ Dual use research of concern
☒	☐ Plants

Methods

n/a	Involved in the study
☒	☐ ChIP-seq
☒	☐ Flow cytometry
☒	☐ MRI-based neuroimaging

Animals and other research organisms

Policy information about studies involving animals; ARRIVE guidelines recommended for reporting animal research, and Sex and Gender in Research

Laboratory animals	Adult male mice of the standard laboratory strain C57BL/6J, with the age of 8-16 weeks were used in this study
Wild animals	No wild animals were used in this study
Reporting on sex	This study focuses on the scientific and hardware system validation of BP-QBC signal transfer method - collection of data from animals with different sex was not needed and/or performed.
Field-collected samples	No field-collected samples were used in the study
Ethics oversight	All the research protocols were approved and monitored by the Purdue University Institutional Animal Care and Use Committee (IACUC), and all research was performed in accordance with relevant NIH guidelines and regulations.

Note that full information on the approval of the study protocol must also be provided in the manuscript.